12.1 THE NCEP NONHYDROSTATIC MESOSCALE FORECASTING MODEL

Zavisa I. Janjic*, Tom L. Black, Eric Rogers, Hui-ya Chuang and Geoff DiMego
National Centers for Environmental Prediction, Camp Springs, Maryland

1. INTRODUCTION

With constantly increasing horizontal resolution, numerical weather prediction models are approaching the limits of validity of the hydrostatic approximation. Although considerable experience with nonhydrostatic models has been accumulated on the scales of convective clouds and storms, numerical weather prediction (NWP) deals with motions on a much wider range of temporal and spatial scales. Difficulties that may not be significant, or may go unnoticed on the small scales, may become important in NWP applications. For example, an erratic gain or loss of mass would be hard to tolerate in an operational environment. Also, problems may arise with the spurious motions generated in the upper levels by the nonhydrostatic dynamics and numerics. Forcing the variables in the top model layers toward a steady state in response to this problem is inadequate for NWP, and, on the other hand, specifying time dependent computational top boundary conditions limits the ability of the nested model to produce more accurate forecasts than the parent model.

Having in mind these considerations, a novel approach (Janjic et al., 2001; Janjic, 2003) has been applied in the NCEP Nonhydrostatic Meso Model (NMM) that has been developed within the Weather Research and Forecasting (WRF) initiative. Namely, instead of extending a cloud model to larger spatial and temporal scales, the hydrostatic approximation is relaxed in a hydrostatic NWP model using vertical coordinate based on hydrostatic pressure. In this way the applicability of the model is extended to nonhydrostatic motions, and at the same time the favorable features of the hydrostatic formulation have been preserved within the range of validity of the hydrostatic approximation.

With this approach the nonhydrostatic equations are split into two parts: (a) the part that corresponds to the hydrostatic system, except for corrections due to the vertical acceleration, and (b) the part that allows computation of the corrections appearing in the first system. The separation of the nonhydrostatic contributions shows in a transparent way where, how and to what extent the hydrostatic approximation affects the equations. The described procedure does not require any linearization or additional approximation.

*Corresponding author address: Zavisa I. Janjic, National Centers for Environmental Prediction, 5200 Auth Rd., Camp Springs, MD 20746; e-mail: Zavisa.Janjic@noaa.gov

2. MODEL EQUATIONS

For simplicity, as a representative of mass based vertical coordinates, consider the sigma coordinate

$$\sigma = \frac{(\pi - \pi_t)}{\mu}, \tag{2.1}$$

where π is the hydrostatic pressure, and μ represents the difference in hydrostatic pressure between the base and the top of the model column

$$\mu = \pi_s - \pi_t . \tag{2.2}$$

Here, π_s and π_t stand for the hydrostatic pressures at the surface and at the top of the model atmosphere. Then, the equations governing a dry, inviscid and adiabatic nonhydrostatic atmosphere are (Janjic et al., 2001; Janjic 2002)

$$\frac{d\mathbf{v}}{dt} = -(1+\varepsilon)\nabla_\sigma \Phi - \alpha \nabla_\sigma p + f\mathbf{k}\times\mathbf{v}, \tag{2.3}$$

$$\frac{\partial T}{\partial t} = -\mathbf{v}\bullet\nabla_\sigma T - \dot\sigma\frac{\partial T}{\partial \sigma} + \frac{\alpha}{c_p}\left(\frac{\partial p}{\partial t} + \mathbf{v}\bullet\nabla_\sigma p + \dot\sigma\frac{\partial p}{\partial\sigma}\right), \tag{2.4}$$

$$\frac{\partial \mu}{\partial t} + \nabla_\sigma\bullet(\mu\mathbf{v}) + \frac{\partial(\mu\dot\sigma)}{\partial\sigma} = 0, \tag{2.5}$$

$$p\alpha = RT, \tag{2.6}$$

$$\frac{1}{\mu}\frac{\partial\Phi}{\partial\sigma} = -\alpha, \tag{2.7}$$

$$w = \frac{1}{g}\left(\frac{\partial \Phi}{\partial t} + \mathbf{v} \bullet \nabla_\sigma \Phi + \dot{\sigma}\frac{\partial \Phi}{\partial \sigma}\right), \qquad (2.8)$$

$$\varepsilon \equiv \frac{1}{g}\frac{dw}{dt}, \qquad (2.9)$$

$$\frac{\partial p}{\partial \pi} = 1 + \varepsilon\,. \qquad (2.10)$$

Here, in the order of appearance, $\mathbf{v}$ is the horizontal wind vector, p is the actual, nonhydrostatic pressure, R is the gas constant for dry air, T is temperature and Φ is geopotential. The other symbols used have either their usual meaning, or their meaning is self-evident. Note that Φ, w, and ε are not independent variables.

The parameter ε is the central point of the extended, nonhydrostatic dynamics. As can be readily verified, if ε is zero, the considered equations reduce to the familiar, hydrostatic system of equations. On the synoptic scales ε is small and approaches the computer round–off error. However, in case of vigorous convective storms, or strong vertical accelerations in the flows over steep obstacles, ε can reach 10^{-3}. For this value of ε the nonhydrostatic deviation of pressure can reach 100 *Pa*. Bearing in mind that the typical synoptic scale horizontal pressure gradient is of the order of 1 *hPa* over 100 *km*, this suggests that significant local nonhydrostatic pressure gradients and associated circulations may develop on small scales. Nevertheless, ε remains much smaller than 1 in atmospheric flows, and therefore, the nonhydrostatic effects are of a higher order magnitude. An important consequence of this situation for the discretization is that high accuracy of computation of ε does not appear to be of paramount importance, since the computational errors are of even higher order than ε.

The method of solving of the system (2.1)-(2.10) is presented in detail in Janjic et al. (2001). Further details and updates are presented in Janjic (2003). Here, only the basic principles of the discretization will be reviewed and the reader is referred to the quoted papers for more details.

3. CLASSICAL NONHYDROSTATIC SOLUTIONS

In order to test the validity of the approach in the limit of highly nonhydrostatic flows, a two-dimensional model in the vertical plane was developed and run in a series of classical nonhydrostatic tests (Janjic et al., 2001). As usual for these scales, the Coriolis force was neglected. As examples, some of the results of Janjic et al. (2001) obtained in the cold and warm bubble tests will be reproduced here. For more details about these and other tests, the reader is referred to Janjic et al. (2001).

Following Straka et al. (1993), in a neutrally stratified atmosphere with the potential temperature of 300^0K, an initial cold disturbance of the form

$$T(x,z) = \overline{T}(x,z) - 15\cos^2\left[\frac{\pi}{2}\sqrt{\left(\frac{x-x_c}{x_t}\right)^2 + \left(\frac{z-z_c}{z_t}\right)^2}\right],$$

$$if \quad \sqrt{\left(\frac{x-x_c}{x_t}\right)^2 + \left(\frac{z-z_c}{z_t}\right)^2} \le 1$$

was introduced, where

$$x_c = 0\ m,\ z_c = 3000\,m,$$
$$x_t = 4000\ m,\ z_t = 2000\,m.$$

The integration domain extended 40 *km* in the x direction, and the free surface was located at 442 *hPa*, or about 6400 *m*. The center of the initial disturbance was in the middle of the domain in the x direction, 20 *km* away from either of the lateral boundaries. As in the main test in the Straka et al. (1993) study, the horizontal resolution was 100 *m*, and the vertical resolution was 100 *m* on the average. The time step was 0.3 *s*.

The potential temperatures after 300 *s*, 600 *s* and 900 *s* are displayed in Fig. 1. The area shown in the

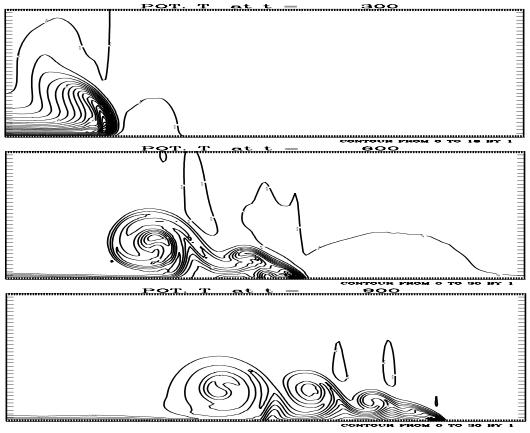

Fig. 1. The cold bubble test. Initial potential temperature and the potential temperatures after 300 *s*, 600 *s* and 900 *s* in the right hand part of the integration domain extending from the center to 19200 *m*, and from the surface to 4600 *m*. The grid size is $\Delta z \approx \Delta x = 100$ *m* and $\Delta t = 0.3$ *s*. The contour interval is 1^0 *K*.

figure extends from the center of the domain to 19200 *m* to the right, and from the surface to 4600 *m*. The contour interval is 1^0 *K*. Comparison of the results obtained in this test (Janjic et al., 2001) with the Straka et al. (1993) converged reference solution reveals very reasonable quantitative and qualitative agreement.

The hydrostatic dynamics was unable to reproduce the results shown in Fig. 1 (Janjic et al., 2001). The hydrostatic solution was computationally unstable unless the lateral diffusion was increased by an order of magnitude. In that case, however, only very crude, qualitative resemblance to the nonhydrostatic solution was preserved.

The warm bubble test was designed following Gallus and Rancic (1996). In a neutral atmosphere with the potential temperature of 300^0K, an initial disturbance of the potential temperature

$$\theta(x,z) = \bar{\theta}(x,z) + 6.6\cos^2\left[\frac{\pi}{2}\sqrt{\left(\frac{x-x_c}{x_t}\right)^2+\left(\frac{z-z_c}{z_t}\right)^2}\right], \quad if \quad \sqrt{\left(\frac{x-x_c}{x_t}\right)^2+\left(\frac{z-z_c}{z_t}\right)^2} \le 1$$

was introduced, where

$$x_c = 0 \ m, \ z_c = 2750\, m,$$
$$x_t = 2500 \ m, \ z_t = 2500\, m.$$

The integration domain extended 20 *km* in the x direction. The free surface was located at 135 *hPa*, or at about 13500 *m*. The center of the initial disturbance was in the middle of the domain in the x direction, i.e., 10 *km* away from either of the lateral boundaries. The horizontal resolution was 100 *m*, and the vertical resolution was 100 *m* on the average. The time step with this spatial resolution was 0.3 *s* as before.

The potential temperature deviation after 360 *s*, 540 *s*, 720 *s* and 900 *s* is presented in Fig. 2. The area shown extends 16 *km* along the x axis, and from 1000 *m* to 13200 *m* along the z axis. The contour interval is 1^0K. The rate of ascent and the intensity of the disturbance agree with those reported elsewhere.

4. HORIZONTAL GRID AND HORIZONTAL COORDINATES

The choice of the horizontal grid is one of the first decisions that has to be made in the process of designing a numerical model of the atmosphere.

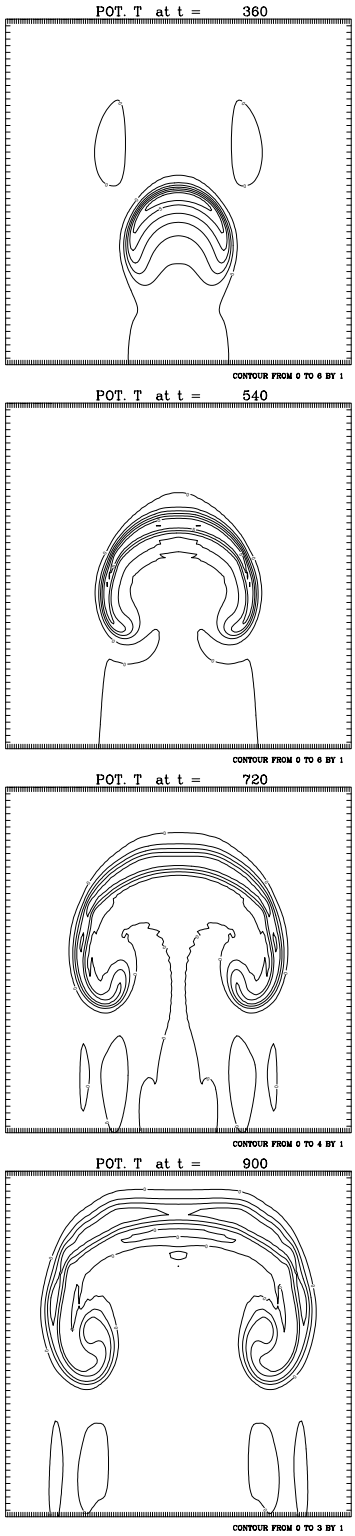

Fig. 2. The potential temperature deviation after 360 *s*, 540 *s*, 720 *s* and 900 *s* (from top to bottom) in the warm bubble test. The area shown extends 16 *km* along the x axis, and from 0 *m* to 13200 *m* along the z axis. The contour interval is 1^0K.

Winninghoff (1968) and Arakawa and Lamb (1977) examined the frequencies of gravity-inertia waves obtained using second-order centered differences on various types of rectangular horizontal grids. According to these studies, compared to other grids considered, generally better agreements with the exact frequencies were obtained on the staggered grid C, and on the semi-staggered grid B (or E) shown in Fig. 3. The

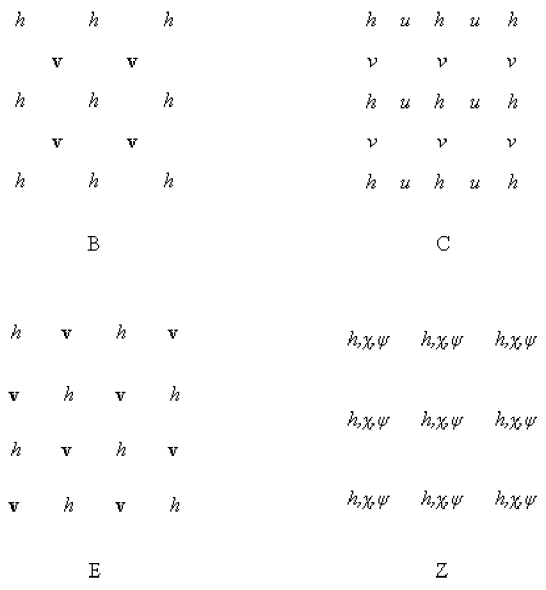

Fig. 3. The staggered grid C and the semi-staggered grids B, E and Z.

symbol h in the figure denotes the mass point variables, while the horizontal velocity vector and the velocity components are denoted, respectively, by $\mathbf{v}$, u and v.

However, the staggered grid and the semi-staggered grids are not without problems, either. The problems on the staggered grid arise due to the averaging of the velocity components in the Coriolis force terms. On the other hand, in order to illustrate the problems on the semi-staggered grids, consider the shallow water equations

$$\frac{\partial u}{\partial t} = -g\frac{\partial h}{\partial x} + fv\,,\quad \frac{\partial v}{\partial t} = -g\frac{\partial h}{\partial y} - fu\,,$$
$$\frac{\partial h}{\partial t} = -H\left(\frac{\partial u}{\partial x} + \frac{\partial v}{\partial y}\right). \qquad (4.1)$$

Here, u and v are the velocity components, h is the height of the free surface, g is gravity, f is the Coriolis parameter assumed to be constant, and H is the mean depth of the fluid. The other symbols used have their usual meaning. The system (4.1) discretized in the most straightforward way, e.g., on the B grid, has the form

$$\frac{\partial u}{\partial t} = -g\delta_x \bar{h}^{y} + fv\,,\quad \frac{\partial v}{\partial t} = -g\delta_y \bar{h}^{x} - fu\,,$$
$$\frac{\partial h}{\partial t} = -H(\delta_x \bar{u}^{y} + \delta_y \bar{v}^{x})\,. \qquad (4.2)$$

In (4.2), the symbol δ and the overbar, respectively, represent the simplest two-point centered differencing and averaging operators applied in the direction indicated by the accompanying subscript or superscript. Following Janjic (1984), the velocity components on the B grid may be written in terms of the velocity potential χ and the stream function ψ in the form

$$u = \delta_x \bar{\chi}^{y} - \delta_y \bar{\psi}^{x}\,,\ v = \delta_y \bar{\chi}^{x} + \delta_x \bar{\psi}^{y}\,. \qquad (4.3)$$

Then, after substituting the expressions (4.3) into the system (4.2), and rearrangement, one obtains

$$\frac{\partial \chi}{\partial t} = -gh + f\psi\,,\ \frac{\partial \psi}{\partial t} = -f\chi\,,$$
$$\frac{\partial h}{\partial t} = -H(\delta_{xx}\bar{\chi}^{yy} + \delta_{yy}\bar{\chi}^{xx})\,, \qquad (4.4)$$

where repeated subscripts and superscripts indicate repeated applications of the operators they are accompanying. As can be seen from (4.4), the only possible reason for the B grid problems is the insufficiently accurate computation of the Laplacian due to the averaging of the derivatives of the velocity potential χ in the continuity equation. An inspection of the finite difference equations (4.4) reveals that they are defined on a nonstaggered grid, carrying all three variables χ, ψ and h at each grid point (Janjic 1984). This type of grid is also shown in Fig. 3. It was named Z grid by Randall (1994). Thus, the B grid, together with the definitions (4.3), is equivalent to the Z grid. However, there is an important difference between the simulation of the gravity-inertia wave propagation on the grids B and Z. On the Z grid, the continuity equation can be written in the form

$$\frac{\partial h}{\partial t} = -H(\delta_{xx}\chi + \delta_{yy}\chi)\,, \qquad (4.5)$$

without averaging in the divergence term that was responsible for the B grid problems. However, an application of the Z grid in case of more complex equations would require costly conversions between the

velocity components and the velocity potential and the stream function.

A more complete comparison of the properties of the remaining two possibilities, the staggered grid C and the semi-staggered grids B and E can be found, e.g., in Janjic and Mesinger (1984, 1989). These considerations, however, do not give decisive advantage to either of the two choices. The problems on the semi-staggered grids B and E are restricted mainly to the shortest waves, while in the case of the slow internal modes, and/or weak stability, the C grid may develop problems in the entire range of the admissible wave numbers (Arakawa and Lamb, 1977). In addition, there is an effective technique for filtering the low frequency, short-wave noise resulting from the inaccurate computation of the divergence term on the semi-staggered grids (Janjic, 1979). More sophisticated, nondissipative methods ("deaveraging" and "isotropisation") for dealing with the problem also have been proposed (Janjic et al., 1998), leading to dramatic improvements of the finite-difference frequencies of the short gravity-inertia waves on the semi-staggered grids.

The results discussed so far are relevant for classical synoptic scale models. In order to address the question of the choice of the horizontal grid as the mesoscales are approached, the linearized anelastic nonhydrostatic system is a better starting point than the linearized shallow water equations (4.1) (communicated by Klemp, 1997; Janjic, 2003).

As before, the problems on the B grid are mainly due to the averaging within the divergence term, and on the C grid mainly due to the averaging of the Coriolis force. For example, if the ratio between the horizontal grid size and the vertical grid size is 30, $f = 0.0001$, the Brunt-Vaisala frequency is $N = 0.0001$, and the wavelength in the vertical is 32 grid intervals, the true relative frequency υ / f, and the relative frequency on the B grid, are both equal to unity throughout the admissible wave number range. On the other hand, as can be seen from Fig. 4, with the same values of the parameters, the relative frequency on the C grid is not a constant. This leads to a nonzero group velocity throughout the admissible wave-number range, including the longest waves. For more details concerning this example, the reader is again referred to Janjic (2003).

On the other hand, the example shown in Fig. 5 indicates how bad the problem can be on the B grid. The two 24 hour sea level pressure forecasts shown in the figure were computed using 30 km horizontal resolution and very light dissipation. The contour

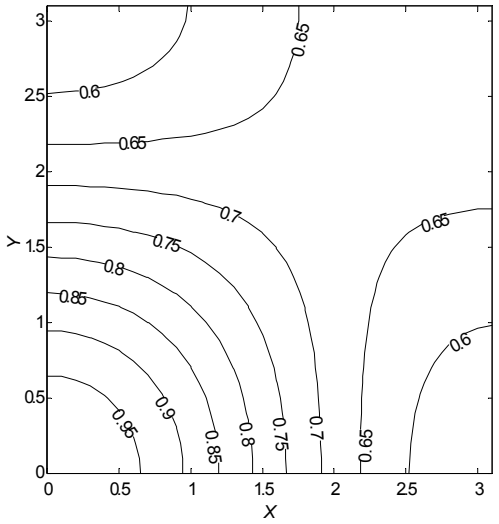

Fig. 4. The ratio υ_C / f as a function of wave number.

interval was set to 1 *HPa* in order to emphasize the noise that might develop. The forecast in the upper panel was obtained doing nothing to alleviate the B grid problem, while the forecast in the lower panel was obtained using the well converged "deaveraging" (Janjic et al., 1998) which substantially improves the frequencies of the gravity-inertia waves on the B grid. As can be seen comparing the forecasts in the upper panel and in the lower panel, the presence of the problem cannot be visually detected. The forecast in the upper panel generally is not noisier than the forecast in the lower panel. This result appears to be in conflict with an earlier result (Janjic, 1979). However, in the earlier test the horizontal resolution was 160 km, so that the advection had a lesser effect in providing communication between the grid points than in the current test with the 30 km resolution.

Since the problems on the semi-staggered grid B are restricted to the shortest resolvable scales, and they are less sensitive to the stability and the choice of the vertical and horizontal grid sizes, the preference was given to the semi-staggered grids. For historical reasons, the E grid is used in the NCEP Nonhydrostatic Meso model (NMM).

The longitude-latitude coordinates are rotated in the model in such a way that the coordinate origin is located in the middle of the integration domain. In this way, the reduction of the longitudinal grid-size is minimized as the southern and the northern boundaries of the integration domain are approached. Thus, generally, longer time steps can be used than on the original longitude-latitude grid.

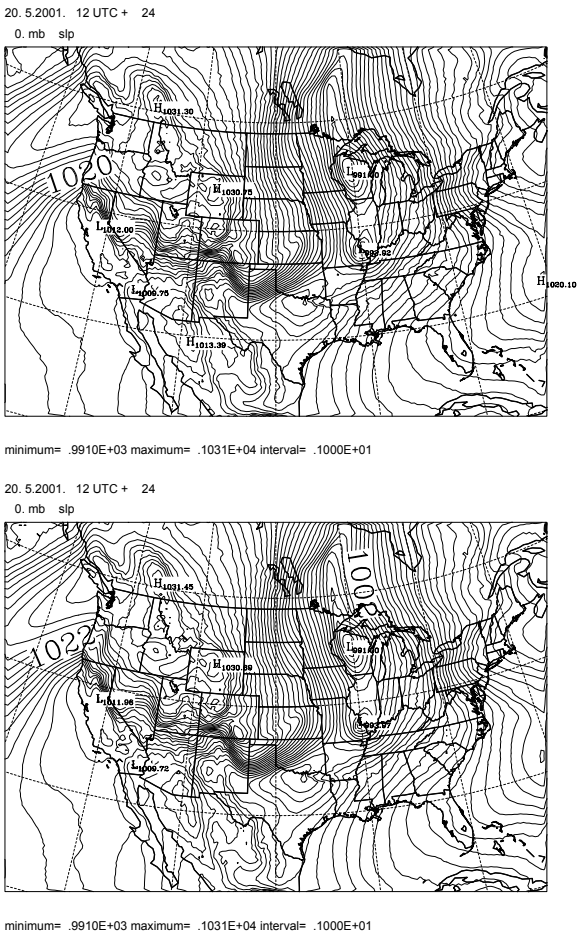

Fig. 5. Examples of 24 hour forecasts of the sea level pressure on the B grid without any attempt to control the grid separation problem (upper panel) and using well converged "deaveraging" (lower panel). The contour interval is 1 *HPa*.

5. VERTICAL COORDINATE AND VERTICAL STAGGERING

By far the most widely used method for representing topography are terrain following coordinates such as the sigma coordinate (Phillips, 1957), or its extensions such as the hybrid sigma-pressure coordinate of Arakawa and Lamb (1977), or the hybrid eta coordinate of Simons and Burridge (1981). A rare exception has been the step-mountain blocking used in the NCEP Meso (Eta) model. Originally proposed by Bryan (1969), and subsequently widely used in oceanography, this technique was implemented in an atmospheric model by Mesinger et al. (1988). Yet another possibility for representation of topography is the shaved cell method (e.g. Adcroft et al. 1997). Steppeler et al. (2002) reported a successful application of this approach in the Local Model (LM) of the German Weather Service.

The advantage of the step-like mountain representation is that the coordinate surfaces are quasi-horizontal. This, however, is not without consequences. For example, internal discontinuities are introduced at the vertical sides of the steps that replace the mountain slopes, and lateral boundary conditions are required at these discontinuities. The formal accuracy of the finite-differences at the points next to the internal boundaries is reduced to the first order. In addition, if the no slip boundary conditions are used in order to preserve the major favorable features of the finite-differencing schemes (Janjic, 1977, 1979, 1984), a nonphysical sink of momentum is introduced. Yet another problem is the representation of the physical processes in the surface layer and the planetary boundary layer (PBL). If one wants to represent these processes in a reasonably uniform way throughout the integration domain, including both low-lying and elevated terrain, an approximately equidistant spacing of the vertical levels is required in the lower few kilometers of the atmosphere. However, the vertical resolution needed in order to achieve this goal is still too high, and otherwise unnecessary. In addition, several recent studies (Adcroft et al, 1997; Gallus, 2000; Gallus and Klemp, 2000; Janjic and DiMego, 2001; Gavrilov, 2002) indicate that more problems should be expected at higher horizontal resolutions.

The shaved cell approach has problems associated with complex lower and internal boundary conditions. In addition, as with the step-mountains, the vertical resolution is reduced over elevated terrain that poses additional problems for physical parameterizations.

Thus, despite of all its imperfections, the terrain-following hybrid pressure-sigma vertical coordinate (Arakawa and Lamb, 1977) has been chosen as the best compromise (Janjic, 2003). With the hybrid coordinate, the coordinate surfaces are flat above and away from the mountains. In the vicinity of the mountains the hybrid coordinate has increased vertical resolution, and the equations are continuous, without the computational internal boundary conditions. Since the hydrostatic pressure is currently used as the vertical coordinate above 400 *hPa*, the possible inaccuracies due to the sloping coordinate surfaces are restricted only to about the lower half of the mass of the atmosphere. Note that, generally, largest errors in the sigma coordinate occur in the stratosphere. Thus, with the hybrid coordinate, the most serious problems associated with the sloping sigma surfaces are eliminated. In addition, the increased resolution presumably acts in the direction of reducing the

computational inaccuracies, and certainly improves the representation of the vertical structure of the PBL over elevated terrain.

The usual, Lorenz vertical staggering of the variables is used in the vertical (Janjic, 1977). The geopotential and the nonhydrostatic pressure are defined at the interfaces of the layers, while all three velocity components and temperature are carried in the middle of the model layers. The vertical velocity is defined at the E grid mass points.

6. SPATIAL DISCRETIZATION

The NMM uses finite differencing with enhanced nonlinear accuracy, as well as other proven major discretization principles applied in the Meso (Eta) model that were proposed by Janjic (1977). Since then, however, the numerical schemes have been further refined. Perhaps the most significant upgrade was the introduction of the new schemes for calculating the contribution of the nonlinear advection terms and the horizontal divergence operators (Janjic, 1984). Properties of the momentum advection scheme were further investigated by Gavrilov and Janjic (1989). In the current model formulation, all divergence operators are computed using the fluxes between each point and its eight nearest neighbors. This, "isotropic", divergence operator is used in the Arakawa Jacobian, but also in the hydrostatic continuity equation in order to compute the divergence of mass.

In the case of rotational flow and cyclic boundary conditions, the scheme for horizontal advection of momentum on the E grid conserves the following properties:

- Enstrophy as defined on the staggred grid C (i.e. using the most accurate second-order approximation of the Laplacian),

$$\sum_{i,j}(\delta_{x'x'}\psi+\delta_{y'y'}\psi)^2\,\Delta A\,, \qquad (6.1)$$

- Rotational kinetic energy as defined on the staggered grid C,

$$\sum_{i,j}\frac{1}{2}(\delta_{y'}\psi)^2\,\Delta A+\sum_{i,j}\frac{1}{2}(\delta_{x'}\psi)^2\,\Delta A\,, \qquad (6.2)$$

- Rotational momentum as defined on the staggered grid C,
- Rotational kinetic energy as defined on the semi-staggered grid E,

$$\sum_{i,j}\frac{1}{2}[\delta_y\psi^2+\delta_x\psi^2]\Delta A\,, \qquad (6.3)$$

- Rotational momentum as defined on the semi-staggered grid E.

The Z grid equivalent of the E grid used to define the quantities (6.1)-(6.3) is shown in Fig. 6 together with the orientation of the coordinate axes x,y and x',y'

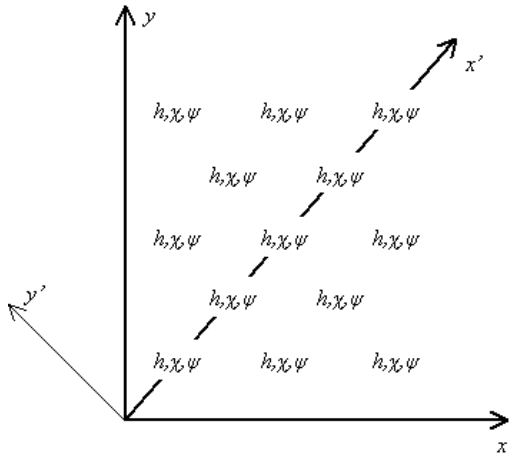

Fig. 6. The Z grid equivalent of the E grid. Orientations of the coordinate axes x,y and x',y' are indicated.

appearing in (6.1)-(6.3). As before, φ and ψ are the velocity potential and the stream function, respectively, and h stands for mass point variables. The symbol ΔA denotes the area of the grid boxes, and the summation sign with the subscripts i,j represents the summation in the horizontal. In case of general flow, the scheme conserves:

- Kinetic energy as defined on the semi-staggered grid E

$$\sum\frac{1}{2}[(\delta_x\varphi-\delta_y\psi)^2+(\delta_y\varphi+\delta_x\psi)^2]\Delta V\,, \qquad (6.4)$$

- Momentum as defined on the semi-staggered grid E.

In (6.4), the summation sign indicates the summation over all grid points, and the symbol ΔV denotes the grid box volume in hydrostatic vertical coordinates.

The scheme for horizontal advection of temperature also conserves the first and the second moments of temperature. Finally, in the hydrostatic limit, when dw/dt tends to zero, the exact cancellation is achieved between the contributions of the pressure gradient force

to the kinetic energy generation, and the $\omega\alpha$ term of the continuity equation, which guarantees consistent transformations between the kinetic and the potential energy, and the conservation of total energy. The relevant finite-difference schemes were presented in Janjic (1977), and their generalizations for the "isotropic", 8-flux divergence operators were discussed in Janjic (1984), and further documented, e.g., in Mesinger et al. (1988).

The exact energy conservation is not currently required in the case of the fully nonhydrostatic equations. In this case the terms involving $\varepsilon = (dw/dt)/g$ are of the order higher than quadratic, and $\varepsilon = (dw/dt)/g$ is small compared to unity in weakly nonhydrostatic flows that can be expected in NWP applications. On the other hand, on the scales, and in the flow regimes where the contribution of $\varepsilon = (dw/dt)/g$ becomes significant, the dissipation starts to play a prominent role creating strong energy sinks.

Two options are available in the model for dealing with the problem of the semi-staggered grids with the frequencies of the short gravity-inertia waves. The first one is the selective filtering technique proposed in Janjic (1979). The second one is the deaveraging technique proposed by Janjic et al. (1998). The deaveraging is computationally very efficient and requires only few simple iterations on the hydrostatic pressure tendency. Although the deaveraging is non-dissipative, and therefore physically better founded, the dramatic improvement of the frequencies of the shortest gravity-inertia waves achieved on the semi-staggered grids requires that the time step be significantly reduced, which leads to reduced computational efficiency of the model. Thus, it is not obvious which of the two options should be given preference in practical NWP applications, particularly in the light of the situation shown in Fig. 5.

Concerning the vertical discretization of the basic dynamical variables, quadratic conservative vertical advection is used. In addition to the material surface boundary conditions requiring that the total derivative of the vertical coordinate (vertical velocity) be equal to zero at the top and at the bottom of the model's atmosphere, vertical boundary conditions are needed for the nonhydrostatic deviation of pressure. It is assumed that the nonhydrostatic pressure deviation vanishes at the top of the atmosphere, while its vertical derivative vanishes at the bottom (Janjic et al., 2001).

The centered conservative schemes used for advection of the basic dynamic variables develop well known problems in case of advection of positive definite scalars with large spatial variation, such as specific humidity, cloud water, or turbulence kinetic energy. For this reason, an upgraded version of the scheme used for advection of passive substances in the NCEP Meso (Eta) model (Janjic, 1997) is applied. The scheme consists of three steps. In the first step an upstream biased scheme is used to advect the passive substance. In the second step, antifiltering is applied, with antifiltering parameters optimized in such a way as to minimize computational dispersion in sheared flows. Finally, in the third step, forced conservation of the advected quantity is imposed. The scheme appears to be a reasonable compromise between the requirements for accuracy and computational efficiency.

7. TIME DIFFERENCING

The hydrostatic core of the system of nonhydrostatic equations (2.1)-(2.10) is split into the following two subsystems (Janjic, 1979; Janjic et al., 2001; Janjic, 2003)

$$(\frac{\partial \mathbf{v}}{\partial t})_i = -\nabla_\sigma \Phi - \alpha \nabla_\sigma \pi + f\mathbf{k}\times\mathbf{v} \qquad (7.1)$$

$$(\frac{\partial T}{\partial t})_i = \frac{\alpha}{c_p}[\mathbf{v}\bullet\nabla_\sigma \pi - \int_0^\sigma \nabla_\sigma \bullet(\mu\mathbf{v})\,d\sigma'] \qquad (7.2)$$

$$(\frac{\partial \mu}{\partial t})_i + \nabla_\sigma \bullet(\mu\mathbf{v}) + \frac{\partial(\mu\dot\sigma)}{\partial\sigma} = 0 \qquad (7.3)$$

$$(\frac{\partial \mathbf{v}}{\partial t})_{ii} = -\mathbf{v}\nabla_\sigma\mathbf{v} - \dot\sigma\frac{\partial\mathbf{v}}{\partial\sigma} \qquad (7.4)$$

$$(\frac{\partial T}{\partial t})_{ii} = -\mathbf{v}\bullet\nabla_\sigma T - \dot\sigma\frac{\partial T}{\partial\sigma} \qquad (7.5)$$

The time derivatives of the two subsystems are denoted by subscripts i and ii, respectively. The systems (7.1)-(7.3) and (7.4)-(7.5) are solved using different time stepping methods. Note that the splitting is not done by separating automatically all the advection terms. Namely, the system with subscripts i includes the advection of pressure in the omega-alpha term of the thermodynamic equation. The contribution of this term compensates the kinetic energy production by the pressure gradient force in the total energy equation. As can be readily verified, due to the presence of this term, the system (7.1)–(7.3), conserves energy. The system (7.4)–(7.5) also conserves energy, except for the changes due to the redistribution of mass.

An economical forward–backward scheme (Ames, 1969; Gadd, 1974; Janjic and Wiin–Nielsen, 1977;

Janjic, 1979) has been used for the system (7.1)–(7.3). The properties of the scheme used in the model were examined in the case of the linearized shallow water equations by Janjic and Wiin–Nielsen (1977) and Janjic (1979). Concerning the contributions of the advection terms (7.4)–(7.5), historically, the split, iterative, first–forward–then–(slightly off–) centered time differencing scheme has been applied with time steps twice longer than those used to solve the subsystem (7.1)–(7.3) (Janjic, 1979). This combination has worked very well in the hydrostatic model on the synoptic scales (Janjic et al., 1995). However, in the nonhydrostatic model, two-grid-interval noise in time develops with this scheme at high resolutions (Janjic, 2003). For this reason, the split two–step iterative scheme for the horizontal advection has been replaced by the nonsplit Adams–Bashforth scheme using the short time step. The Adams–Bashforth scheme allows about the same computational efficiency as the two–step, iterative scheme with twice longer time steps, and the accuracy is improved. However, somewhat more memory is needed in order to store some of the variables at the third time level, and the physical mode of the Adams–Bashforth scheme is weakly unstable. This instability can be tolerated if the time steps are not too long, or can be eliminated by a very slight off-centering which preserves the second order accuracy. Note that large ratios between the advection time step, and the time step used for the remaining terms of the equations cannot be used in NWP applications. This ratio is restricted to only about 2 on the semi-staggered grids, where longer short steps can be used than those allowed by the CFL criterion on the staggered grid C.

The trapezoidal scheme for the Coriolis force terms has been also recently replaced by the Adams-Bashforth scheme. The reason for this change was the possibility of overestimating the amplitude of the divergent part of flow with the trapezoidal scheme (Janjic and Wiin-Nielsen, 1977).

For simplicity, the time differencing has been presented using only the hydrostatic part of the model dynamics. The treatment of the contribution of the nonhydrostatic dynamics is more involved, and the details on the time stepping procedures used can be found in Janjic et al. (2001) and Janjic (2003). A novelty in the treatment of the nonhydrostatic terms is that the iterative method for solving the vertical implicit pressure equation discussed in Janjic et al. (2001) has been replaced by a direct solver (Janjic, 2003). This modification has brought a visible further improvement of the computational efficiency of the model. Currently, the passive substance transport remains the single most expensive part of the model dynamics.

8. FIRST EXPERIENCES IN OPERATIONAL APPLICATIONS

Since July 2002, the NMM has been run operationally in NCEP HiRes windows in six nested domains (Western, Central, Eastern, Alaska, Hawaii, Puerto Rico) shown in Fig. 7. The physical package is similar to that of the NCEP Meso (Eta) model (Janjic, 1990, 1994, 1996, 2000, 2002; Chen et al., 1997), although certain upgrades have been introduced. The horizontal resolution is 8 *km* for all domains except for the Alaska domain where the horizontal resolution is 10 km. The model has 60 unequally spaced levels.

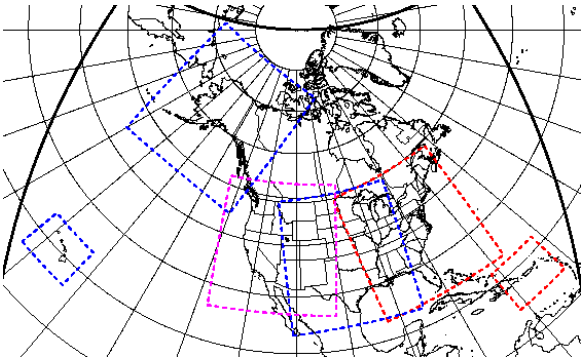

Fig. 7. The six HiRes Windows: Western, Central, Eastern, Alaska, Hawaii and Puerto Rico.

The model topography is defined as unfiltered gridbox means of 30'' USGS Digital Elevation Model data. The model does not have its own dedicated data assimilation system. The initial and boundary conditions are defined by interpolation of the operational Meso (Eta) model data. The Meso (Eta) model is run with 12 *km* resolution and 60 levels in the vertical.

In the two small domains (Hawaii and Puerto Rico) the model is run twice a day (starting from 00 UTC and 12 UTC, and 06 UTC and 18 UTC, respectively). In the remaining four domains, the model is run once a day starting from 00 UTC (Alaska), 06 UTC (Western), 12 UTC (Central) and 18 UTC (Eastern). The forecasts are computed up to 48 hours.

The computational efficiency of the model has been very high, and substantially higher than the computational efficiency of most established nonhydrostatic models. Moreover, further significant improvement of the computational efficiency of the model is possible. Also, the model has been highly reliable and there has been no failed runs since the operations started.

In terms of performance on the synoptic scales, generally, the model has been highly competitive with mature high-resolution NWP models, despite the fact that it has been handicapped by inconsistent initial and

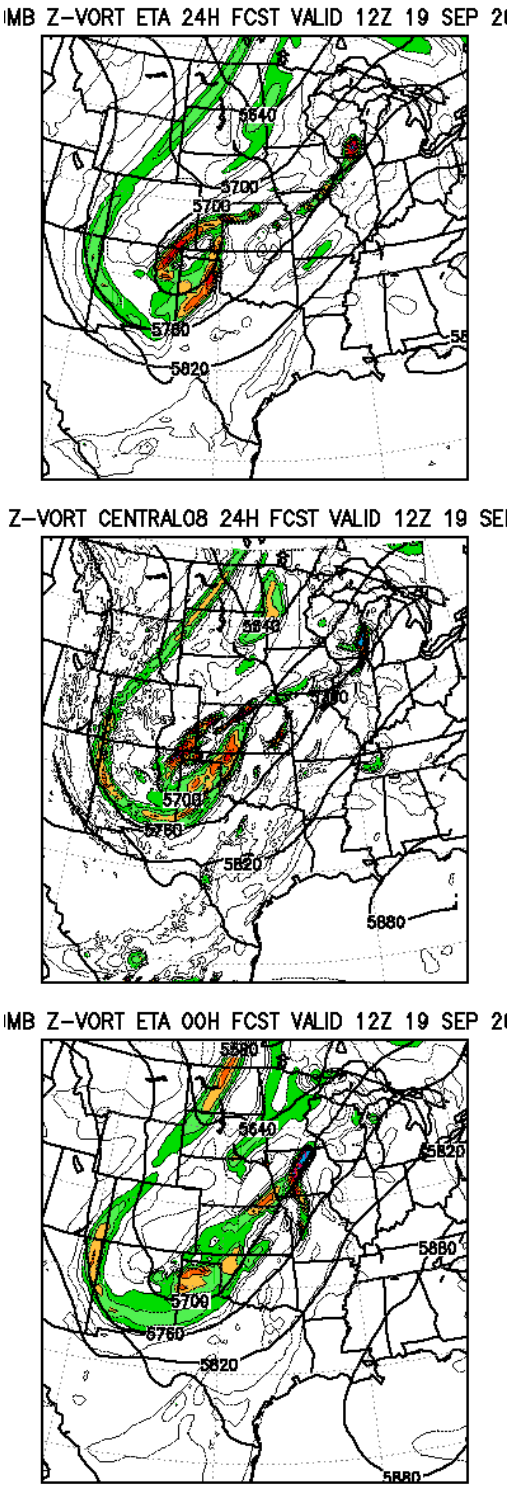

Fig. 8. A case of cyclogenesis in the lee of the Rockies. The 24 hour forecasts of the 500 hPa height obtained using the operational Meso (Eta) model with 12 *km* resolution (top panel) and with the NMM with 8 *km* resolution in the Central domain (middle panel), and the verifying Meso (Eta) EDAS analysis (bottom panel).

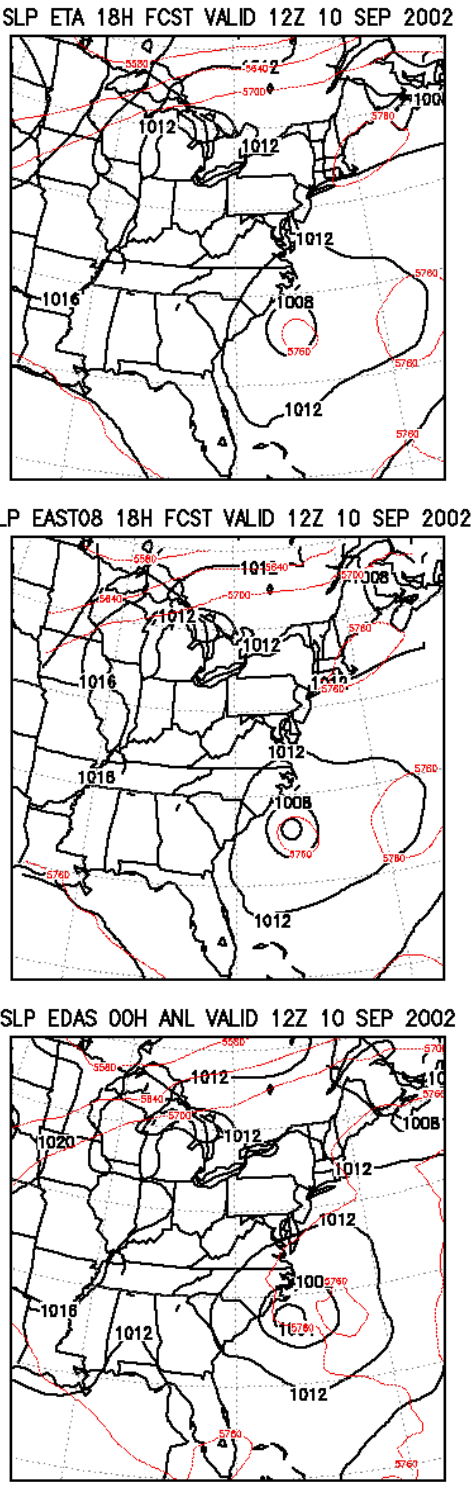

Fig. 9. A case of a tropical storm. The 18 hour forecasts of the sea level pressure obtained using the operational Meso (Eta) model with 12 *km* resolution (top panel) and with the NMM with 8 *km* resolution in the Eastern domain (middle panel), and the verifying Meso (Eta) EDAS analysis (bottom panel).

boundary conditions, relatively small integration domain and almost no physics retuning. Several examples will be presented here in order to illustrate the potentials of the current system. Further examples can be found in (Black et al., 2002).

The 24 hour forecasts of the 500 *hPa* height in a case of cyclogenesis in the lee of the Rockies obtained using the operational Meso (Eta) model with 12 *km* resolution (top panel), and with the NMM with 8 *km* resolution in the Central domain (middle panel), as well as the verifying Meso (Eta) EDAS analysis (bottom panel) are shown in Fig. 8. As can be seen from the figure, the operational Meso (Eta) model developed a cut-off low that did not verify in the analysis, while the development predicted by the NMM (middle panel) was in a better agreement with the observations.

As another example, 18 hour forecasts of the sea level pressure in a case of a tropical storm obtained using the operational Meso (Eta) model with 12 *km* resolution (top panel) and with the NMM with 8 *km* resolution in the Eastern domain (middle panel), as well as the verifying Meso (Eta) EDAS analysis (bottom panel) are shown in Fig. 9. The operational Meso (Eta) model developed the cyclone that was too shallow. In

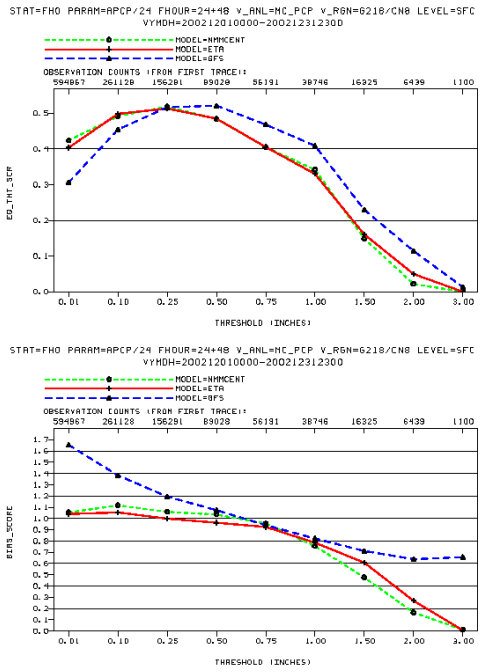

Fig. 10. The precipitation scores for January 2003 for the 12 *km* operational Meso (Eta) model (solid red line) and the embedded 8 *km* NMM in the Central domain (dashed green line) are shown in Fig. 9. The monthly mean threat scores (upper panel) and bias scores (lower panel) for accumulated 24 hour precipitation at 24 and 48 hour forecast times are presented.

contrast to that, the depth of the cyclone predicted by the NMM agreed very well with the verifying Meso (Eta) analysis.

The precipitation scores for January 2003 for the 12 km operational Meso (Eta) model (solid red line) and the embedded 8 km NMM in the Central domain (dashed green line) are shown in Fig. 10. The monthly mean threat scores (upper panel) and bias scores (lower panel) for accumulated 24-hour precipitation at 24 and 48 hour forecast times are presented. The Central

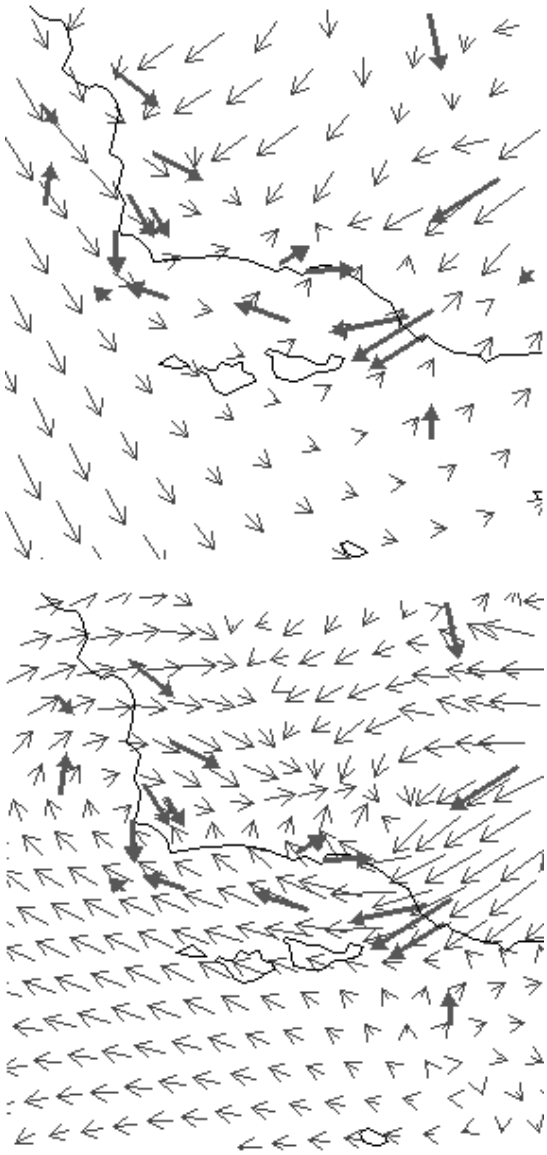

Fig. 11. The 42 hour forecasts of 10 m wind for the Santa Barbara area, California, valid at 00UTC, February 6, 2003. The forecast obtained using the 12 *km* Meso (Eta) model is shown in the upper panel, and the forecast from the 8 *km* NMM Western domain run is shown in the lower panel.

domain has very diverse geography, ranging from highest and steepest mountains to vast plains and water covered areas. As can be seen from the figure, the two models scored about equally well.

In addition to the precipitation scores, the bias and RMS errors are computed for several variables using radiosonde data valid at 00 UTC and 12 UTC for verification (not shown). Although the scores vary with time, generally, they remain comparable for the two models. The differences in the scores remain within the limits one would expect considering the differences in the specification of the initial and boundary conditions, domain sizes, resolution and tuning.

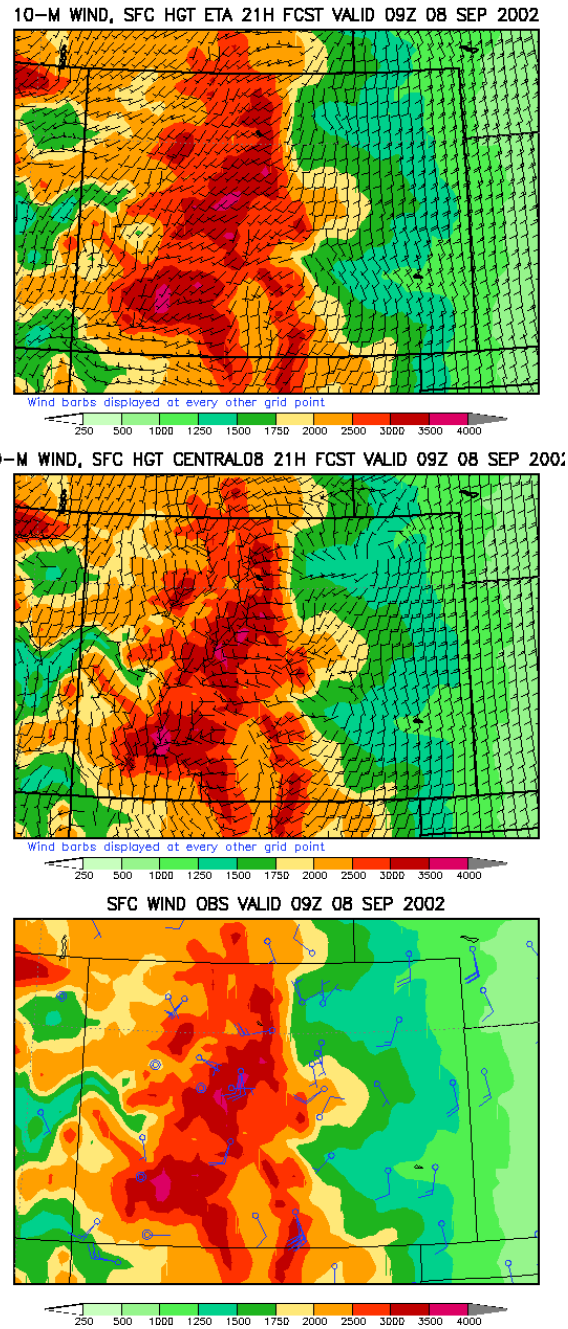

Fig. 12. Examples of 21 hour 10 m wind forecasts in Colorado valid at 09 UTC September 8, 2002 using the 12 *km* Meso (Eta) (top panel) and the 8 *km* NMM Central domain (middle panel), and the verifying observations (bottom panel).

More significant differences between the two models can be seen in details. For example, consider the 42 hour forecasts of 10 *m* wind for the Santa Barbara area, California, valid at 00 UTC, February 6, 2003 that are shown in Fig. 11. The forecast obtained using the 12 *km* Meso (Eta) model is shown in the upper panel, and the forecast from the 8 *km* NMM Western domain run is shown in the lower panel. The bold arrows represent the observations. As can be seen from the figure, generally, there is a much better agreement between the NMM forecast and the observations. In particular, the northeast low level jet that turns to east and southeast over the ocean in the Oxnard area is realistically reproduced in the NMM forecast, while it is completely missing in the Meso (Eta) forecast.

Another example of a 10 *m* wind forecast, this time from Colorado, is presented in Fig. 12. The 12 *km* Meso (Eta) (upper panel) and the 8 *km* NMM Central domain (middle panel) 21 hour forecasts valid at 09 UTC September 8, 2002, are shown together with the verifying observations (bottom panel). As can be seen from the plots, in contrast to the Meso (Eta) model, the NMM successfully reproduced two small vortices in Denver and Pueblo areas.

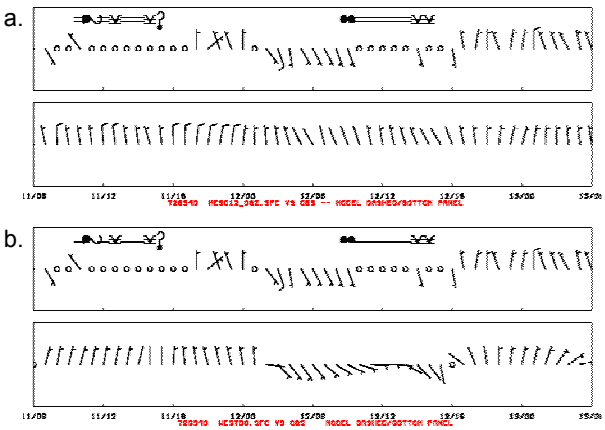

Fig. 13. The 48 hour time series of forecast (lower plot) and verifying 10 *m* winds (upper plot) for the Meso (Eta) model (a.) and the NMM (b.).

A similar situation was observed on February 12, 2003 in Salem, Oregon. The 48 hour time series of forecast (lower plot) and verifying 10 *m* winds (upper

plot) are shown in Fig. 13 for the Meso (Eta) model (a.) and the NMM (b.). As can be seen from the observations, during the 48 hour forecast period, the wind changed the direction from north to south, and then again, from south to north. In contrast to that, the Meso (Eta) maintained the northerly wind throughout the forecast. On the other hand, the NMM successfully reproduced the change of the wind direction at approximately the right time.

The most dramatic differences between the two models, however, can be seen in the vertical structure of mountain waves. An example is shown in Fig. 14.

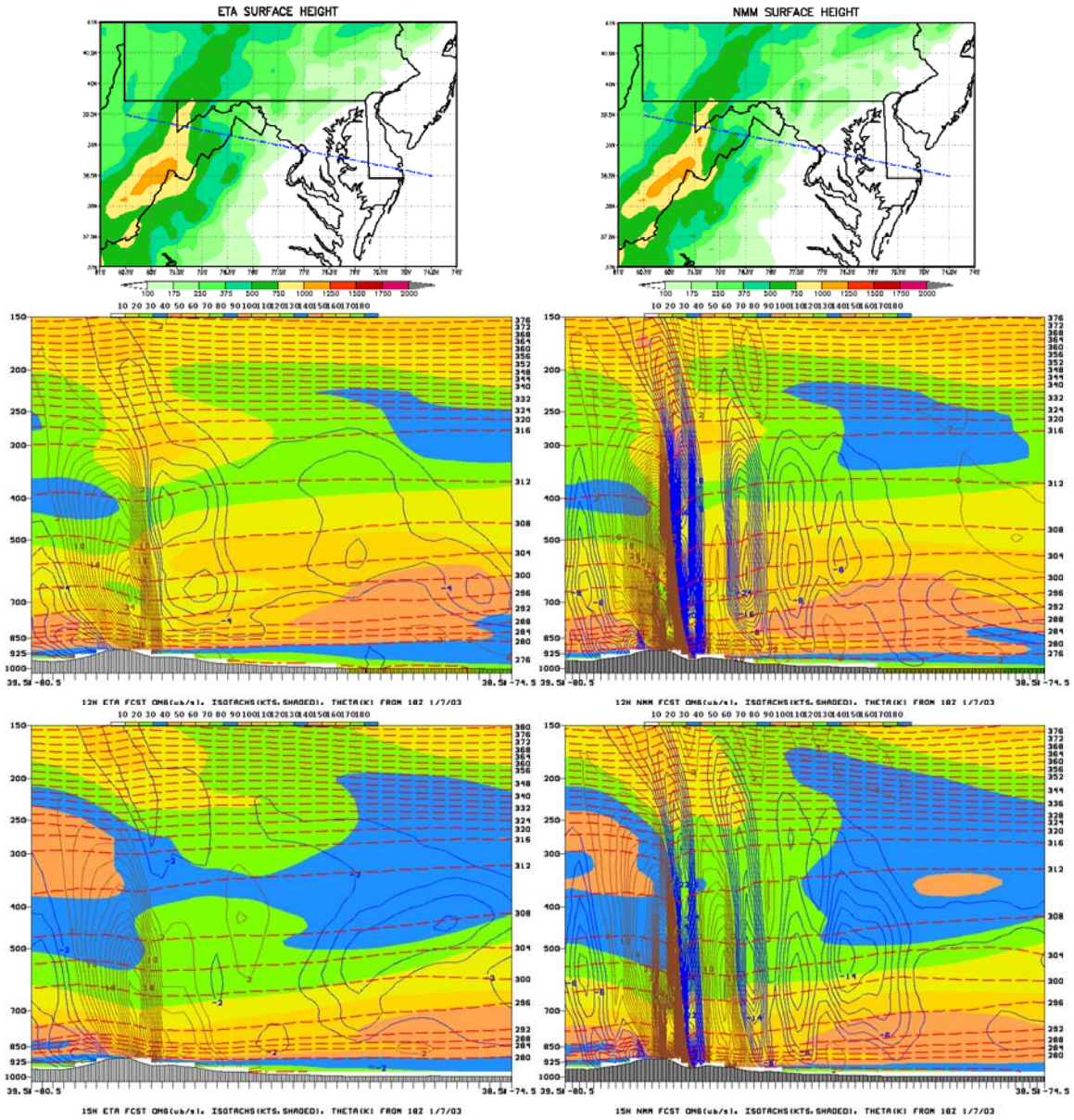

Fig. 14. The 12 *km* Meso (Eta) (left column) and the 8 *km* NMM Eastern domain (right column) cross sections. The middle and bottom panels of the columns are 12 hour and 15 hour forecast cross sections, respectively, starting from 18 UTC, January 7, 2003. The cross sections are taken along the blue lines in the top panels. The topography is indicated in the top panels by color shading with the contours at 100, 175, 250, 375, 500, 750, 1000, 1250 etc. meters, and by the shaded area at the bottom of the cross sections. The blue and brown contour lines are the negative (upward) and positive (downward) values of vertical velocity $\omega = dp/dt$, respectively. The contour interval is 0.2 *Pa s*$^{-1}$. The dashed red contour lines are potential temperature with the contour interval of 4 degrees. The background color shading in the cross sections represents isotachs with the contour interval of 10 *Knts*.

The panels in the column on the left hand side are from the 12 *km* Meso (Eta) run, and the panels in the column on the right hand side are from the 8 *km* NMM Eastern domain run. The middle and the bottom panels of the two columns represent the 12 hour and the 15 hour forecast cross sections, respectively, starting from 18 UTC, January 7, 2003. The cross sections are taken along the blue lines in the top panels. The topography is indicated in the top panels by color shading with the contours at 100, 175, 250, 375, 500, 750, 1000, 1250 etc. meters, and by the shaded area at the bottom of the cross sections. The blue and brown contour lines indicate the negative (upward) and positive (downward) values of vertical velocity $\omega = dp/dt$, respectively. The contour interval is 0.2 *Pa* s^{-1}. The potential temperature is represented by the dashed red contour lines with the contour interval of 4 degrees. The background color shading in the cross sections represents isotachs with the contour interval of 10 *Knts.*

As can be seen from the figure, the vertical motions are much stronger in the NMM than in the Meso (Eta) model. Moreover, the wave length of the mountain waves in the NMM is much shorter than in the Meso (Eta) model. In addition to the resolution, the representation of mountains and the nonhydrostatic dynamics are believed to have played a role in producing so different results.

9. CONCLUSIONS

The NCEP nonhydrostatic meso model (NMM) (Janjic et al., 2001; Janjic, 2003) has been formulated building on the experiences of high resolution hydrostatic numerical weather forecasting. In this way, the favorable features of the hydrostatic formulation are preserved in the range of validity of the hydrostatic approximation.

The basic idea applied was to split the system of the nonhydrostatic equations into two parts: (a) the part that corresponds basically to the hydrostatic system, except for higher order corrections due to the vertical acceleration, and (b) the system of equations that allows computation of the corrections appearing in the first system due to the vertical acceleration. This procedure does not require any linearization or additional approximation.

The nonhydrostatic dynamics is introduced through an add–on module. The separation of the nonhydrostatic contributions shows in a transparent way where, how, and to what extent relaxing the hydrostatic approximation affects the familiar hydrostatic equations. The nonhydrostatic module can be turned on and off, so that the same model can be run in both hydrostatic and nonhydrostatic modes. This allows easy comparison of hydrostatic and nonhydrostatic solutions of otherwise identical model. This feature also allows that the model be run in the hydrostatic mode at lower resolutions with no extra cost. This is an advantage in case of models designed for a wide range of horizontal resolutions, and in particular for unified global and regional forecasting systems.

At very high resolutions, a two-dimensional version of the model successfully reproduced the classical nonhydrostatic solutions (Janjic et al., 2001). Although such resolutions will not be affordable in NWP applications in the near future, it was necessary to pass this test in order to demonstrate the soundness of the formulation. At the very small scales, the hydrostatic and the nonhydrostatic solutions were substantially different. The nonhydrostatic model was generally more robust than the hydrostatic one, and produced smoother solutions.

The extra computational cost due to the nonhydrostatic extension is of the order of 20% of the cost of the hydrostatic dynamics. The relatively low cost of the nonhydrostatic dynamics justifies the application of the nonhydrostatic model even at medium resolutions. Compared to the hydrostatic version of the model, no additional computational boundary conditions have been needed in real data runs in a wide range of horizontal resolutions.

The NMM has become operational at NCEP in July of 2002 and has demonstrated remarkable skill (Black et al., 2002). In real data runs, it does not require additional computational boundary conditions at the top.

The computational efficiency of the model has been very high, and substantially higher than the computational efficiency of most established nonhydrostatic models. Moreover, further significant improvement of the computational efficiency of the model is possible. The model has been highly reliable and there has been no failed runs since the operations started.

In terms of performance on the synoptic scales, generally, the model has been highly competitive with mature high resolution NWP models, despite the fact that it has been handicapped by inconsistent initial and boundary conditions, relatively small integration domain, and almost no retuning of the physical parameterizations.

More significant differences between the NMM and the NCEP hydrostatic high resolution Meso (Eta) model can be seen on smaller scales. The differences are particularly striking in meso scale vertical structures developed by the two models.

Although the initial results have been very encouraging, further efforts are needed in order to develop full potentials of the model. This applies

primarily to retuning of the physical parameterizations that are currently biased towards the step-mountain representation. Faster progress in this respect has been hampered by a lack of resources at NCEP that has been further aggravated by the problems associated with migration to the new computers.

References

Adcroft, A., C. Hill and J. Marshall, 1997: Representation of topography by shaved cells in a height coordinate ocean model. *Mon. Wea. Rev.*, **125**, 2293–2315.

Arakawa, A. and V. R. Lamb, 1977: Computational design of the basic dynamical processes of the UCLA general circulation model. *Methods in Computational Physics, 17, Academic Press*, 173-265.

Black, T., E. Rogers, Z. Janjic, H. Chuang, and G. DiMego, 2002: Forecast guidance from NCEP's high resolution nonhydrostatic mesoscale model. 15th Conf. on NWP, San Antonio, TX, Amer. Meteor. Soc., J23-J24.

Bryan, K., 1969: A numerical method for the study of the circulation of the World Ocean. *J. Comp. Phys*, **4**, 347-376.

Chen, F., Z. Janjic and K. Mitchell, 1997: Impact of atmospheric surface–layer parameterization in the new land–surface scheme of the NCEP mesoscale Eta model. *Boundary–Layer Meteorology* **48**, 391–421.

Gallus W. A., Jr., 2000: The Impact of Step Orography on Flow in the Eta Model: Two Contrasting Examples. *Wea. and Forecasting*, **15**, 630–639.

Gallus W. A., Jr. and J. B. Klemp, 2000: Behavior of Flow over Step Orography. *Mon. Wea. Rev.,* **128**, 1153–1164.

Gallus, W.A. and M. Rancic, 1996: A non-hydrostatic version of the NMC's regional Eta model. *Q. J.R. Meteorol. Soc.*, **122**, 495-513.

Gavrilov, M. B., 2002: Comments on "A More Extensive Investigation of the Use of Ensemble Forecasts for Dispersion Model Evaluation". *J. Appl. Meteorol.,* **41**, 899.

Gavrilov, M. B. and Z. I. Janjic, 1989: Computed rotational energy spectra of two energy and enstrophy conserving schemes on semi-staggered grids. *Meteorol. Atmos. Phys.,* **41**, 1-4.

Janjic, Z. I., 1977: Pressure gradient force and advection scheme used for forecasting with steep and small scale topography. *Contrib. Atmos. Phys.*, **50**, 186–199.

_____, 1979: Forward–backward scheme modified to prevent two–grid–interval noise and its application in sigma coordinate models. *Contrib. Atmos. Phys.*, **52**, 69–84.

_____, 1984: Non–linear advection schemes and energy cascade on semi–staggered grids. *Mon. Wea. Rev.*, **112**, 1234–1245.

_____, 1990: The step–mountain coordinate: physical package. *Mon. Wea. Rev.*, **118**, 1429–1443.

_____, 1994: The step–mountain eta coordinate model: further developments of the convection, viscous sublayer and turbulence closure schemes. *Mon. Wea. Rev.*, **122**, 927–945.

_____, 1996: The surface layer in the NCEP Eta model. 11th Conf. on NWP, Norfolk, VA, Amer. Meteor. Soc., 354–355.

_____, 1997: Advection scheme for passive substances in the NCEP Eta model. Research Activities in Atmospheric and Oceanic Modelling, WMO, Geneva, CAS/JSC WGNE, 3.14.

_____, 2000: Comments on "Development and Evaluation of a Convection Scheme for Use in Climate Models. *J. Atmos. Sci.*, **57**, p. 3686

_____, 2002: Nonsingular Implementation of the Mellor-Yamada Level 2.5 Scheme in the NCEP Meso model. NCEP Office Note No. 437, 61 pp.

_____, 2003: A Nonhydrostatic Model Based on a New Approach. *Meteorol. Atmos. Phys.*, **82**, 271-285.

Janjic, Z. and A. Wiin–Nielsen, 1977: On geostrophic adjustment and numerical procedures in a rotating fluid. *J. Atmos. Sci.*, **34**, 297–310.

Janjic, Z. I. and F. Mesinger, 1984: Finite-difference methods for the shallow water equations on various horizontal grids. *Numerical Methods for Weather Prediction,* Vol. 1, Seminar, ECMWF, 1983, Reading, U.K., 29-101, Shinfield Park, Reading, Berkshire RG2 9AX, U.K.

Janjic, Z. I. and F. Mesinger, 1989: Response to small-scale forcing on two staggered grids used in finite-difference models of the atmosphere. *Quarterly Journal of the Royal Meteorological Society,* Vol. **115**, 1167-1176.

Janjic, Z. I., F. Mesinger and T. L. Black, 1995: The pressure advection term and additive splitting in split-explicit models. *Quarterly Journal of the Royal Meteorological Society,* Vol. **121**, No. 524, 953-957.

Janjic, Z. I., J. P. Gerrity, Jr. and S. Nickovic, 2001: An Alternative Approach to Nonhydrostatic Modeling. *Mon. Wea. Rev.*, **129**, 1164-1178.

Janjic, Z. I., and G. DiMego, 2001: Effects of Mountain Representation and Nonhydrostatic Dynamics in a Case of Orographic Precipitation. Symposium on Precipitation Extremes: Prediction, Impacts and Responses. 81st Annual Meeting of the Amer. Meteor. Soc., January 14-19, 2001, Albuquerque, NM, AMS, Boston, MA, 24-28.

Mesinger, F., Z.I. Janjic, S. Nickovic, D. Gavrilov and D.G. Deaven, 1988: The step–mountain coordinate: model description and performance for cases of Alpine lee cyclogenesis and for a case of an Appalachian redevelopment. *Mon. Wea. Rev.*, **116**, 1493–1518.

Phillips, N.A., 1957: A coordinate system having some special advantages for numerical forecasting. *J. Meteor.*, **14**, 184-185.

Randall, D. A., 1994: Geostrophic Adjustment and the Finite-Difference Shallow-Water Equations. *Mon. Wea. Rev.,* **122**, 1371–1380.

Simmons, A. J., and D. M. Burridge, 1981: An energy and angular-momentum conserving vertical finite-difference scheme and hybrid vertical coordinates. *Mon. Wea. Rev.*, **109**, 758-766.

Steppeler, Jürgen, Heinz-Werner Bitzer, Maud Minotte, Luca Bonaventura, 2002: Nonhydrostatic Atmospheric Modeling using a *z*-Coordinate Representation. *Mon. Wea. Rev.*, **130**, 2143–2149.

Straka, J.M., R.B. Wilhelmson, L.J. Wicker, J.R. Anderson and K.K. Droegemeier, 1993: Numerical solutions of a non-linear density current: a benchmark solution and comparisons. *Intl. J. Numerical Methods in Fluids*, **17**, 1-22.

Winninghoff, F. J., 1968: On the adjustment toward a geostrophic balance in a simple primitive equation model with application to the problems of initialization and objective analysis. Ph. D. Thesis, *Dept. Meteor. Univ. California*. “Dept. Meteor. Univ. California, Los Angeles, CA 90024, U.S.A.”